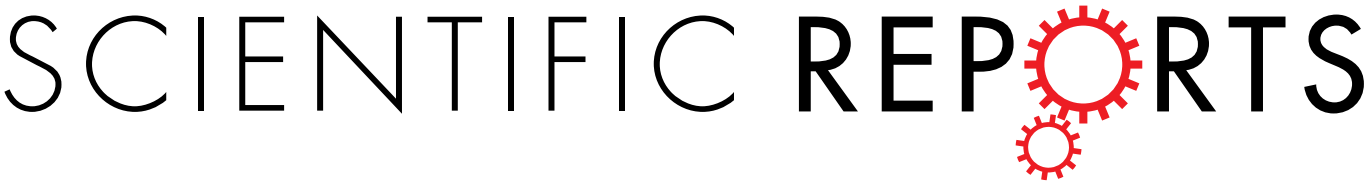

OPEN

Thermodynamic and microstructural study of Ti_2AlNb oxides at 800 °C

Received: 8 February 2018
Accepted: 14 August 2018
Published online: 24 August 2018

J. M. Xiang[1], G. B. Mi[2], S. J. Qu[1], X. Huang[2], Z. Chen[1,3], A. H. Feng[1], J. Shen[1] & D. L. Chen[4]

The high-temperature structural applications of Ti_2AlNb-based alloys, such as in jet engines and gas turbines, inevitably require oxidation resistance. The objective of this study is to seek fundamental insight into the oxidation behavior of a Ti_2AlNb-based alloy via detailed microstructural characterization of oxide scale and scale/substrate interface after oxidation at 800 °C using X-ray diffraction (XRD), scanning electron microscopy (SEM), electron probe microanalysis (EPMA), and transmission electron microscopy (TEM). The oxide scale exhibits a complex multi-layered structure consisting of (Al,Nb)-rich mixed oxide layer (I)/mixed oxide layer (II)/oxygen-rich layer (III)/substrate from the outside to inside, where the substrate is mainly composed of B2 and O-Ti_2AlNb phases. High-resolution TEM examinations along with high-angle annular dark-field (HAADF) imaging reveal: (1) the co-existence of two types (α and δ) of Al_2O_3 oxides in the outer scale, (2) the presence of metastable oxide products of TiO and Nb_2O_5, (3) an amorphous region near the scale/substrate interface including the formation of $AlNb_2$, and (4) O-Ti_2AlNb phase oxidized to form Nb_2O_5, TiO_2 and Al_2O_3.

Ti_2AlNb-based alloy, sometimes referred to as orthorhombic alloy[1,2], is a class of highly promising lightweight high-temperature materials. This type of alloy is considered to partially substitute the high-density ($\rho = 8\sim8.5$ g/cm^3) Ni-based superalloys in the aerospace industry due to its low density, high strength, superior plasticity, high fracture toughness and excellent creep resistance at elevated temperatures[3–9]. In such applications, the operating temperatures could go beyond 600–650 °C[10,11], leading to severe oxidation of the alloy surface[12–14]. There are three potential approaches to improve high-temperature oxidation resistance: alloying[15–17], pre-oxidation[18], and coating[19–26]. For example, Wang *et al.*[27] reported that a two-step voltage-controlled microarc oxidation (MAO) method can be used to produce ceramic coatings on a Ti_2AlNb-based alloy. However, after a prolonged exposure to air at elevated temperatures, intermetallics exhibit oxygen-induced embrittlement characteristics such as low ductility and brittle fracture[16,28,29]. Thus, an understanding of high-temperature oxidation mechanisms is essential for improving the oxidation resistance of materials. In our previous study[30], a Ti_2AlNb-based alloy was observed to exhibit fairly good oxidation resistance below 750 °C. After reaching 800 °C, the oxidation resistance decreased dramatically. Thus, the oxidation behavior and mechanisms are investigated at a higher temperature of 800 °C in this study.

Mass transfer is known to be the essence of oxidation reaction. During the high-temperature oxidation of a Ti_2AlNb-based alloy, O and N elements diffuse inward, whereas Al, Ti and Nb elements diffuse outward. Among the many elements that can improve the oxidation resistance, such as Al, Nb, Mo, Si, Zr, etc., Al and Nb are the most important elements[31]. While Al atoms and O atoms are able to generate a continuous and dense Al_2O_3 protective layer on the alloy surface and thus improve the oxidation resistance of alloys, this is not the case in Ti_2AlNb-based alloys. The Gibbs free energy of Al_2O_3 and TiO_2 is so similar that both oxides are produced almost simultaneously[32]. The addition of the element Nb can improve the oxidation resistance of the alloy: Nb substitutes for Ti in TiO_2 as a cation with a valence of 5, while no Nb is present in Al_2O_3[33–37]. The doping of Nb in TiO_2 grains reduces oxygen vacancy and Ti cations, which impedes the mass transfer in TiO_2[34]. Lu *et al.*[35] observed the substitution of Ti by Nb via high-resolution transmission electron microscopy (HRTEM) Z-contrast imaging, as

[1]School of Materials Science and Engineering, Tongji University, Shanghai, 201804, P.R. China. [2]Aviation Key Laboratory of Science and Technology on Advanced Titanium Alloys, AECC Beijing Institute of Aeronautical Materials, Beijing, 100095, China. [3]Aerospace Hiwing (Harbin) Titanium Industrial Co., Ltd., Harbin, 150028, China. [4]Department of Mechanical and Industrial Engineering, Ryerson University, Toronto, Ontario, M5B 2K3, Canada. Correspondence and requests for materials should be addressed to S.J.Q. (email: qushoujiang@tongji.edu.cn) or D.L.C. (email: dchen@ryerson.ca)

represented by the Nb enrichment in TiO_2 grains of the mixture layer. Vojtěch *et al.*[36] studied the role of the addition of 2 at.% Nb to the eutectic TiAl-Ti_5Si_3 alloy, and reported that Nb markedly influences oxidation kinetics, with a six-fold decrease of oxidation rate.

Some fundamental aspects of oxidation behavior, such as weight gain, scale morphology, and structure, have been investigated[12,21,38–41]. Leyens and Gedanitz[12] studied the mass gain and oxidation rate of a Ti-22Al-25Nb alloy in air between 650 °C and 800 °C, and reported a fairly good oxidation resistance at 650 °C up to 4000 hours and at 700 °C up to 500 hours, whereas at 800 °C "breakaway" oxidation occurred after about 100 hours. Wang *et al.*[21] observed layers of TiO_2 and a small amount of $AlNbO_4$ with needle-like TiO_2 crystals present all over the surface. Ralison *et al.*[38,39] reported a multi-layered scale ($TiO_2 + \frac{1}{2}AlNbO_4$/(eventually Ta, Mo) − rich $AlNbO_4$) along with an oxygen-affected zone in a Ti-27Al-15Nb alloy at 800 °C in air, and Al_2O_3/($TiO_2 + AlNbO_4$)/Ta-rich Al_2O_3/oxygen-affected zone in a Ti-27Al-10Nb alloy at the same temperature of 800 °C. Some cracks were present in the multi-layered scale. Zheng *et al.*[40] studied the oxidation behavior of a Ti-22Al-25Nb alloy at 800 °C for 300 hours and observed the formation of a mixed oxide scale on the alloy surface, which was predominantly composed of TiO_2, $AlNbO_4$, and Nb_2O_5.

These studies revealed a complex scale structure containing oxidation products of Al_2O_3, TiO_2, Nb_2O_5, $AlNbO_4$, etc., with an outer layer consisting mainly of TiO_2. When the content of the element Nb is high enough, Nb_2O_5 or $AlNbO_4$ would be present, however, they are prone to spall-off and are unfavorable to the oxidation resistance. As for the structure of inner oxide layer, Małecka[41] observed that it consists of an Al-rich layer and Ti, Al (Nb, Mo, V)-rich zone. Li *et al.*[42] reported that it has such a structure: TiO_2-rich layer/$AlNbO_4$-rich layer/TiO_2-rich layer/$AlNbO_4$-rich layer/oxygen and a nitride-enriched zone. Leyens[14] reported that when the temperature is above 900 °C there exists a nitrogen-enriched layer underneath the oxide scale, i.e., a nitride-containing layer. However, the questions remain as to how the oxide scale containing various oxides is formed; in what form (crystalline or amorphous) the substance/scale interface region would be; and if different types of Al_2O_3 can be co-existent in the oxidation of Ti_2AlNb-based alloys. The objective of the present study is to address these questions via detailed microstructrual examinations using different advanced techniques along with thermodynamic calculations.

Materials and Methods

The selected material is as-cast Ti_2AlNb alloy with a nominal composition of Ti-22Al-20Nb-2V-1Mo-0.25Si (in at.%). The alloy ingot was cut into small plates with a size of 8 × 8 × 3 mm by electro-discharge machining. The surface of the samples was ground with sandpaper from grit #400 to #1200, ultrasonically cleaned in acetone for 15 mins. The dimensions were measured using a Vernier caliper and the samples were weighted using an analytical balance with an accuracy of 0.00001 g. During the isothermal oxidation in air at 800 °C, the samples were taken out of the furnace at intervals of 1, 3, 6, 12, 24, 36, 50, 62, 74, 86, and 100 h, cooled to room temperature and weighed. It should be noted that the Ti_2AlNb-based alloy was observed to exhibit a fairly good oxidation resistance below 750 °C, while its oxidation resistance decreased considerably above 800 °C. Thus, the oxidation behavior and mechanism are studied in detail at 800 °C in the present investigation. The time of oxidation experiments was selected according to the standard HB5258-2000 of aerospace sector in China, where a duration of 100 hours is suggested to be sufficient. Also, if the oxidation time was too long, the oxide layer would peel off, causing difficulties for the study of the oxide scale.

A stereoscope was used to observe the grain sizes. XRD (Rigaku D/Max-2550) with a Cu K_α radiation ($\lambda = 1.5418$ Å) was used to identify the phases in the oxide scale at 50 kV and 200 mA with a diffraction angle (2θ) from 10° to 100° at a step size of 0.02° and 1 s in each step. SEM (Nova Nano SEM 450) was used to observe the surface morphology and cross-sectional structure of the oxide layer. For the observation of the oxide cross-section, it was necessary to mount the sample with resin, use sandpapers from grit #400 to #1200 to grind, and then diamond paste to polish the sample to a smooth mirror surface. Since the oxide is an insulator, it is necessary to perform carbon deposition on the polished surface before SEM observations. Elemental distribution in different regions on the cross-section of the oxide scale was characterized by using an electron probe microanalyzer (EPMA, Shimadzu 1720) with a resolution of 1 μm and secondary-electron image resolution of 6 nm using a beam current of 10 nA. TEM (FEI TECNAI G2 S-TWIN F20) was used to examine the structures of the oxide scale as well as the scale/substrate interface. To locate the scale/substrate interface more precisely TEM samples were prepared via the cutting of a focused ion beam (FIB, FEI, Helios nanolab 600). The dimension of FIB-TEM samples is: 5 μm in length, 4 μm in width, ~35 nm in thickness for the scale, and ~65 nm in thickness for the scale/substrate interface.

Results

Microstructures of as-cast Ti_2AlNb alloy. Ti_2AlNb-based alloy contains different volumes of the ordered phases β_0 (Strukturbericht: B2, space group: $Pm\bar{3}m$, Person symbol: cP2), α_2-Ti_3Al (Strukturbericht: DO_{19}, space group: $P6_3/mmc$, Pearson symbol: hP8), and the ordered orthorhombic O-Ti_2AlNb phase (Strukturbericht: A_2BC, space group: CmCm, Person symbol: oC16)[43]. There exist crystallographic orientations of these phases[1–3]: $[1\bar{1}1]_{B2}//[11\bar{2}0]_{\alpha_2}$, $(011)_{B2}//(0001)_{\alpha_2}$, $[0001]_{\alpha_2}//[001]_O$, $(10\bar{1}0)_{\alpha_2}//(110)_O$, $[\bar{1}11]_{B2}//[1\bar{1}0]_O$, $(110)_{B2}//(001)_O$. X-ray diffraction pattern, stereoscopic image, back-scattered electron (BSE) SEM micrograph, and TEM bright field image along with the relevant selected area electron diffraction (SAED) patterns of as-cast Ti_2AlNb alloy are shown in Fig. 1(a–g). XRD results reveal the presence of O-Ti_2AlNb phase, B2 phase, and α_2 phase in Fig. 1(a). The stereoscopic image indicates coarse grains in the Ti_2AlNb-cast alloy (Fig. 1(b)). The SEM image in Fig. 1(c) shows dark α_2 phase, gray O-Ti_2AlNb phase and B2 phase, which can be better seen in a magnified TEM image in Fig. 1(d). In Fig. 1(c), a small amount of α_2 phase is mainly located at grain boundaries in the Ti_2AlNb-based

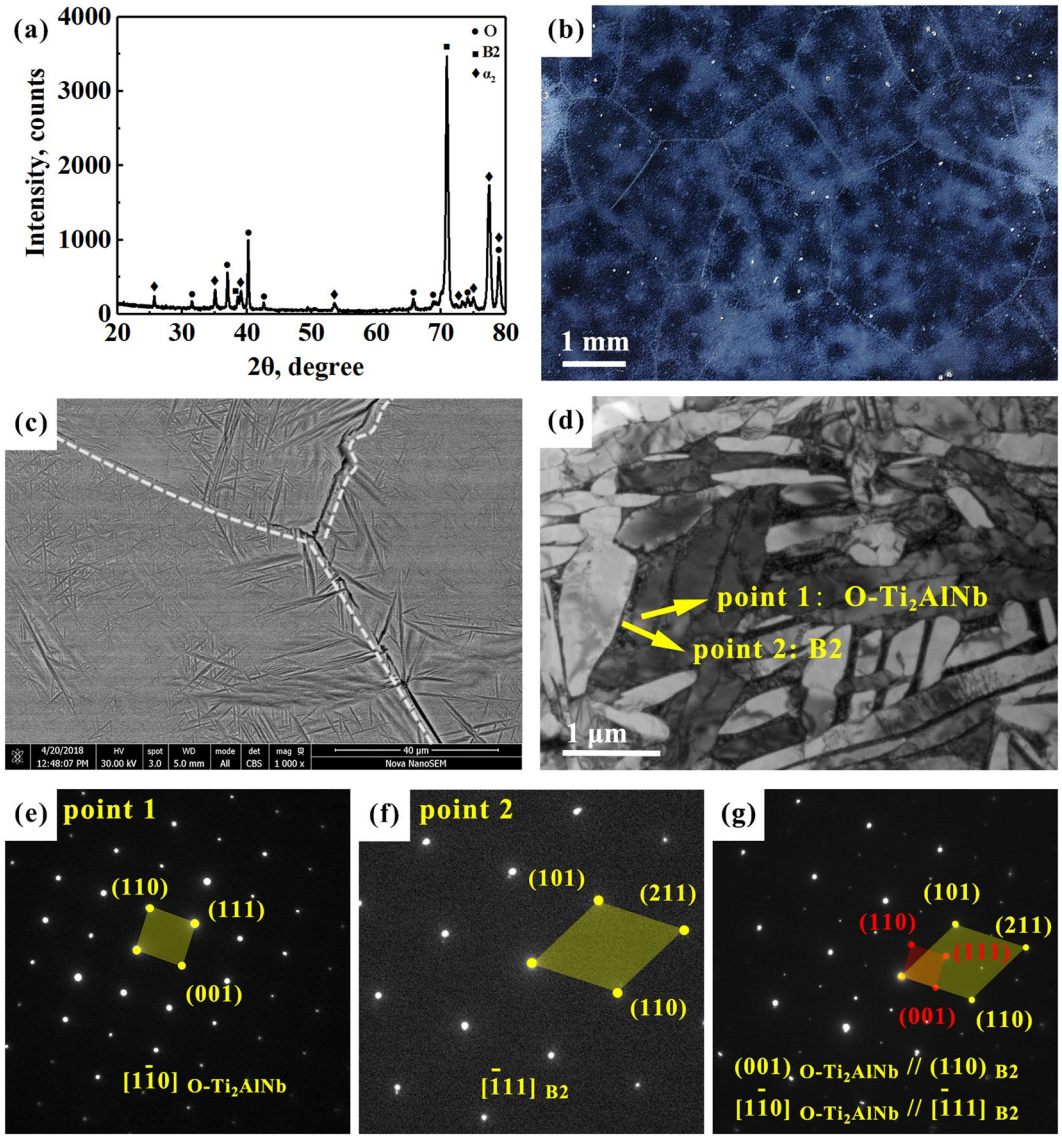

Figure 1. X-ray diffraction pattern (**a**) and microstructure (**b**–**g**) of as-cast Ti_2AlNb-based alloy. (**b**) Stereoscopic image showing coarse grains; (**c**) SEM back-scattered electron micrograph showing dark α_2-Ti_3Al, gray B + O-Ti_2AlNb phases; (**d**) TEM bright field image along with (**e**–**g**) the corresponding SAED patterns of points 1 and 2, and crystallographic orientations, where 1 stands for O-Ti_2AlNb phase, and 2 denotes B2 phase.

alloy. Then there are only B2 phase (matrix) and O-Ti_2AlNb phase (lath) presented in Fig. 1(d–g), with crystallographic orientations between them: $[\bar{1}11]_{B2}//[1\bar{1}0]_O$, $(110)_{B2}//(001)_O$.

Isothermal oxidation kinetics. Figure 2(a) shows a curve of isothermal oxidation kinetics of Ti_2AlNb-cast alloy at 800 °C. The obtained weight gain of this alloy after 100 h at 800 °C was about 9.3 mg/cm^2. The relationship between oxidation and mass gain could be obtained by fitting the experimental data using the following equation,

$$\Delta M^n = k_n t, \tag{1}$$

where ΔM represents the weight gain per unit area (mg/cm^2), n is an oxidation exponent ($n = 1$, liner relationship; $n = 2$, parabolic relationship), k_n is a rate constant (mg^n/cm^{2n}·h), and t is oxidation time (h). The obtained oxidation exponent was ~0.83, being close to 1, thus suggesting that the oxidation kinetics of Ti_2AlNb-cast alloy at 800 °C obeyed basically a linear relationship and the oxide layer is not protective at this temperature.

Surface morphology and structure of scale. Secondary electron micrograph, XRD pattern, back-scattered electron SEM micrograph, and EPMA mapping are shown in Fig. 2(b–e). Randomly-oriented and fairly-dense laminar-shaped oxides of about 2~3 μm long are observed to cover the alloy surface, as seen in Fig. 2(b).

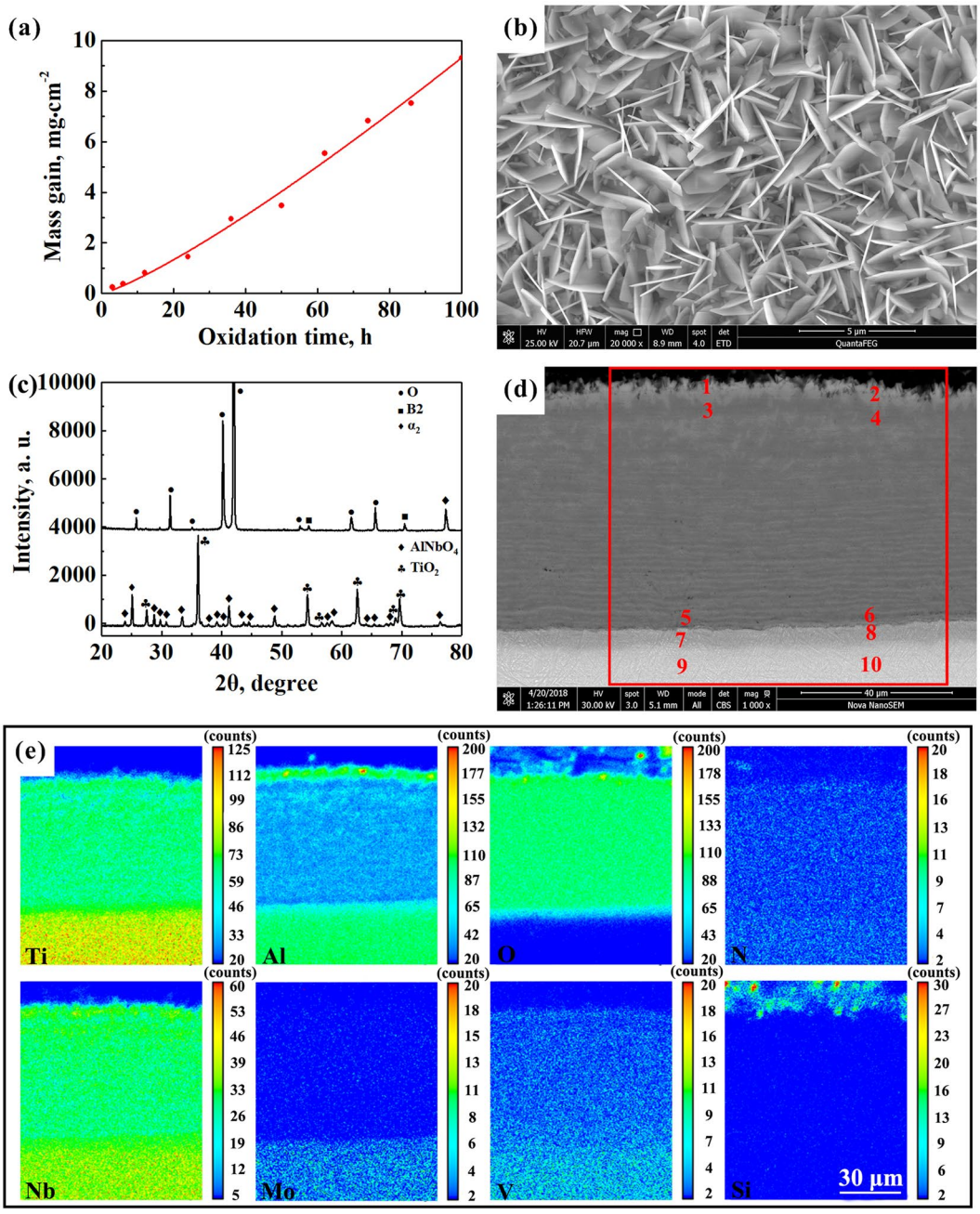

Figure 2. Oxidation of Ti_2AlNb-cast alloy at 800 °C for 100 h. (**a**) Oxidation kinetics; (**b**) surface morphology of scale; (**c**) XRD pattern of the oxide scale on the surface and substrate; (**d**) SEM back-scattered electron micrograph of cross-structure scale; (**e**) EPMA mapping of a selected area in (**d**).

X-ray diffraction patterns of oxide scale on Ti_2AlNb alloy are shown in Fig. 2(c). It is seen that a large amount of $AlNbO_4$ and TiO_2 is present in the scale after oxidation at 800 °C. According to our previous studies[30], the laminar-shaped oxide is $AlNbO_4$. The cross-section of the overall scale can be seen from an SEM back-scattered electron (BSE) image shown in Fig. 2(d). The scale appears dense with a thickness of ~60 μm, and it consists of three layers based on the EPMA mapping in Fig. 2(e). The structure can be deduced to be (Al,Nb)-rich mixed oxide layer (I)/mixed oxide layer (II)/oxygen-rich layer (III) from the outside to inside. However, the presence of some Al_2O_3 is also found in layer I through TEM investigations.

EPMA point microanalyses were used to reveal the chemical composition in various locations of the cross-sectional scales in Fig. 2(d). According to XRD results in Fig. 2(c) and the chemical composition of points 1–10 in Table 1, $AlNbO_4$ and TiO_2 can be confirmed to be the main oxides in the scale. However, Al and Nb are richer at points 1–2 (in the outermost scale of ~5 μm thick) than at points 3–6, i.e., the (Al,Nb)-rich mixed outer layer (I) and mixed mid-layer (II). This should be a result of the rapid growth of TiO_2. The consumption of oxygen leads to a reduction in the oxygen partial pressure, but there is still sufficient oxygen (compared to the interior of

Number	Ti	Al	Nb	Mo	V	Si	O	N
1	11.88	12.03	11.64	0.00	0.93	0.03	63.50	0.00
2	12.75	11.04	12.26	0.00	0.96	0.03	62.96	0.00
3	22.56	5.63	6.82	0.00	0.61	0.03	62.92	1.43
4	23.41	5.22	6.59	0.00	0.64	0.05	62.66	1.43
5	23.40	5.52	6.86	0.00	0.97	0.07	61.73	
6	21.28	6.63	7.72	0.00	0.92	0.11	62.15	1.19
7	34.09	12.01	13.28	0.20	1.38	0.16	34.35	4.52
8	36.66	12.59	14.15	0.24	1.58	0.21	29.07	5.51
9	43.29	16.02	14.84	0.22	1.67	0.20	17.54	6.23
10	44.93	15.92	16.85	0.26	1.82	0.18	14.51	5.54

Table 1. Elemental composition (at.%) determined via EPMA at points 1–10 in Fig. 2(d).

the alloy) in the O-rich zone (III), as represented by points 7–10 where the content of oxygen was determined to be ~15 at.% or higher, as shown in Table 1. Also, a low content of nitrogen indicates that there is no nitride present in the oxide scale (points 1–6). N and O penetrated into O-rich zone (III) will cause an environmental brittleness and reduce the mechanical properties of the alloy[28].

TEM study of oxide layer. TEM samples were taken from the outer scale (right) and at the scale/substrate interface (left) via FIB, as shown in Fig. 3(a). Figure 3(b) shows a TEM bright-field image, with the SAED pattern of point 1 given in Fig. 3(c), indicating the presence of $AlNbO_4$ phase. Figure 3(d) is an HRTEM image of point 2 in Fig. 3(b), where Fourier transformations of 2A, 2B, and 2 C were performed to obtain diffraction patterns shown in Fig. 3(e) to (g), corresponding to α-Al_2O_3, δ-Al_2O_3 and α-Al_2O_3. This suggests the co-existence of different types of Al_2O_3 oxides. It should be noted that, to the best of the authors' knowledge, such a co-existent phenomenon of different forms of Al_2O_3 oxides observed via HRTEM has not been reported in the literature, where α-Al_2O_3 is a thermodynamically stable form (corundum form) while δ-Al_2O_3 is one of metastable transition forms/polymorphs of alumina. Figure 3(h) is a SAED pattern of point 3 in Fig. 3(b), which corroborates the presence of TiO_2.

Figure 4 shows the microstructures of interface between Ti_2AlNb substrate and oxide scale, from a TEM sample taken at the interface of oxide layer/substrate (i.e., the left TEM sample shown in Fig. 3(a)). Figure 4(a,b) present a TEM bright-field image and a high angle annular dark-field (HAADF) image, respectively, where the left side represents the substrate and the right side represents the oxide scale. It should be noted that the white spots in the oxide layer in Fig. 4(a) are pores. The rutile-TiO_2 is found at point 1 in Fig. 4(c,d), with an amorphous surrounding. Nb content at point 2 is very high, and it has been identified as $AlNb_2$ (Fig. 4(e)), which is also one of the common oxidation products of the Ti_2AlNb-based alloy. Point 3 shows a TiO polycrystalline ring (Fig. 4(f)), which is further oxidized to become TiO_2. In Fig. 4(g,h) for point 4, Nb_2O_5 is revealed to be present at the boundary of two phases. This is due to the fact that the diffusion of oxygen at the phase boundary is faster as a result of the presence of phase (or grain) boundary energy, along with the reduced reaction activity of Ti and Al. Point 5 shows a lamellar O-Ti_2AlNb phase where brookite TiO_2 and O-Ti_2AlNb phases are present, which are shown in Fig. 4(i). In Fig. 4(j), TiO_2, γ-Al_2O_3, and Nb_2O_5 are observed to co-exist in the O-Ti_2AlNb laths, with the orientation relationships of γ-Al_2O_3 and TiO_2: $(211)_{\gamma-Al_2O_3}//(220)_{rutile-TiO_2}$, $(003)_{\gamma-Al_2O_3}//(112)_{rutile-TiO_2}$, $[1\bar{2}0]_{\gamma-Al_2O_3}//[1\bar{1}0]_{rutile-TiO_2}$.

Discussion

Evolution of B2 phase and O-Ti_2AlNb phase. As mentioned above, the Ti_2AlNb-based alloy consists of 3 phases, i.e., α_2-Ti_3Al, B2, and O-Ti_2AlNb. In the present Ti_2AlNb-cast alloy there is fewer α_2-Ti_3Al phase existing in the vicinity of grain boundaries and the O-Ti_2AlNb laths are present in the original coarsened B2 grains. The diffusion rate of oxygen atoms in the B2 phase is larger than that in the other two phases[44]. It follows that no B2 phase is present at the interface. This means that oxidation reaction occurs first in the B2 phase, producing metastable TiO, which is further oxidized to TiO_2. The brightest regions on the HAADF image in Fig. 4(b) are Nb-rich areas and have been identified to be $AlNb_2$. It is sandwiched between the complete and residual O-Ti_2AlNb laths, which corresponds to the former position of the B2 phase. $AlNb_2$ is considered as a by-product during the oxidation of the Nb-containing TiAl-based alloy, which is due to the reaction of enriched Nb and Al elements[45]. There are a large number of Nb element in the B2 phase[43]. During oxidation, the Ti element in the B2 phase reacts with the O element to form TiO/TiO_2. The consumption of Ti causes the reaction of Al and Nb. As a result, $AlNb_2$ is surrounded by gray TiO/TiO_2 in Fig. 4(b). $AlNb_2$ is stably present at the interface, indicating that its oxidation resistance is relatively strong[45], however, the discontinuous nature of $AlNb_2$ at the interface makes the effect limited.

After this the O-Ti_2AlNb phase is oxidized. Combined with Fig. 4(f–j), there are brookite-TiO_2, rutile-TiO_2, γ-Al_2O_3, and Nb_2O_5 in the O-Ti_2AlNb phase. It can thus be considered that the O-Ti_2AlNb phase has been oxidized and decomposed into oxides of TiO_2, Al_2O_3, and Nb_2O_5. Al_2O_3 blocks the transport channel, hinders further growth of TiO_2, and improves oxidation resistance. As one of the oxide products, Al_2O_3 has been reported extensively in the literature. During the early stage of oxidation, the oxides at the interface exist in an amorphous form. Lu *et al.*[29] reported that polycrystalline TiO_2 and amorphous Al_2O_3 coexist in the scale. This is similar to the structure in Fig. 4(c). It should be noted that TiO_2 and Al_2O_3 occur almost simultaneously because of their similar

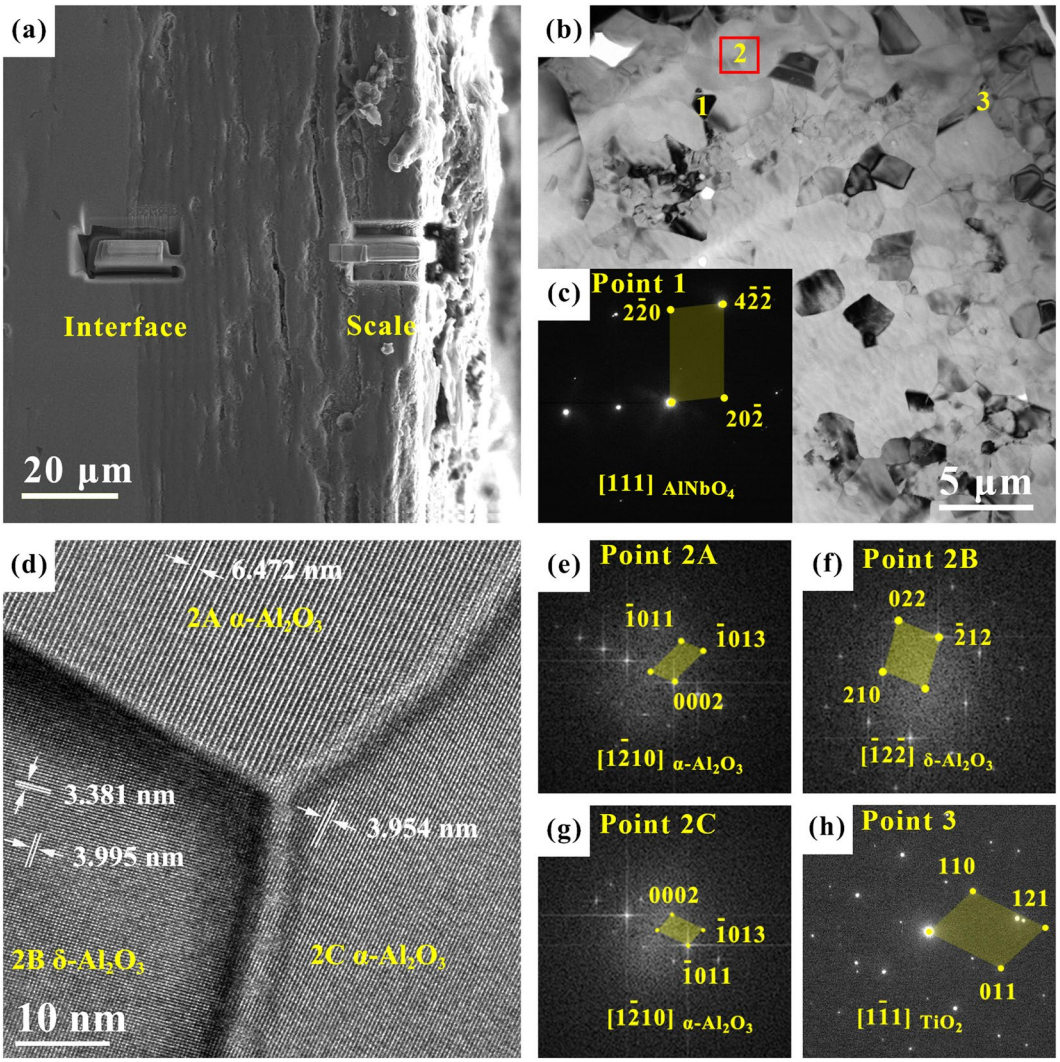

Figure 3. Analysis of oxide scale after oxidation at 800 °C for 100 h. (**a**) Position of TEM samples prepared via FIB; (**b**) TEM bright field image; (**c**) and (**h**) the corresponding SAED patterns of point 1 and 3 in (**b**), and (**d**–**g**) the corresponding HRTEM and FFT images of point 2 in (**b**), where 1 represents $AlNbO_4$, 2 A denotes α-Al_2O_3, 2B stands for δ-Al_2O_3, 2 C signifies α-Al_2O_3, and 3 indicates rutile-TiO_2.

Gibbs free energy[43], however, the energy is not high enough at an oxidation temperature of 800 °C, resulting in the presence of metastable alumina. To the best of the authors' knowledge, there is no report about the structure of Al_2O_3 in the oxidation of a Ti_2AlNb-based alloy. In the present work, the unique formation of alumina is observed via HRTEM in the alloy after oxidation at 800 °C for 100 h. That is, the presence of three adjoining oxide grains and oxides in O-Ti_2AlNb laths, as shown in Figs 3(d) and 4(j), suggests the occurrence of phase change among three types of Al_2O_3, i.e., α-Al_2O_3, δ-Al_2O_3, and γ-Al_2O_3. The γ-Al_2O_3, θ-Al_2O_3, and κ-Al_2O_3 are common metastable phases in TiAl alloys at 900 °C[29,46,47]. According to Yang *et al.*[48], γ-Al_2O_3 formed with twins in the oxidation of NiAl, and γ-Al_2O_3 twins were observed to play an important role in the scale growth. Cowley *et al.*[49] reported that {111} γ-Al_2O_3 twin boundaries provide a fast diffusion path for Al cations. This would improve the oxidation resistance of an alloy. However, in the present study of the Ti_2AlNb-based alloy at 800 °C, there exists δ-Al_2O_3 (monoclinic, $a = 11.74$ Å, $b = 5.72$ Å, $c = 11.24$ Å, $\beta = 103.34°$[50]), while no γ-Al_2O_3 twins are observed. As reported by Levin and Brandon[51], there is a route for the formation of Al_2O_3: Amorphous (anodic film) → γ → δ → θ → α-Al_2O_3. This would be the phase change route of Al_2O_3 in the present Ti_2AlNb-based alloy. Further studies in this aspect are needed at different oxidation temperatures.

Formation of $AlNbO_4$. As described above, there are TiO_2, Al_2O_3, and $AlNbO_4$ in the outer oxide layer, as presented in Fig. 3. Zheng *et al.*[40] assumed that the fast-growing Nb_2O_5 could react with Al_2O_3 that developed at the early stage of oxidation to form $AlNbO_4$. In the present work, Dmol3 module in Materials Studio 6.0 is used to calculate the Gibbs free energy change of reaction: $Nb_2O_5 + Al_2O_3 \rightarrow 2AlNbO_4$, however, the temperature in the software is up to 1000 K only, which is lower than the temperature of the present oxidation experiment, 1073.15 K. Thus, the following equation is used to fit the relationship between the Gibbs free energy and temperature,

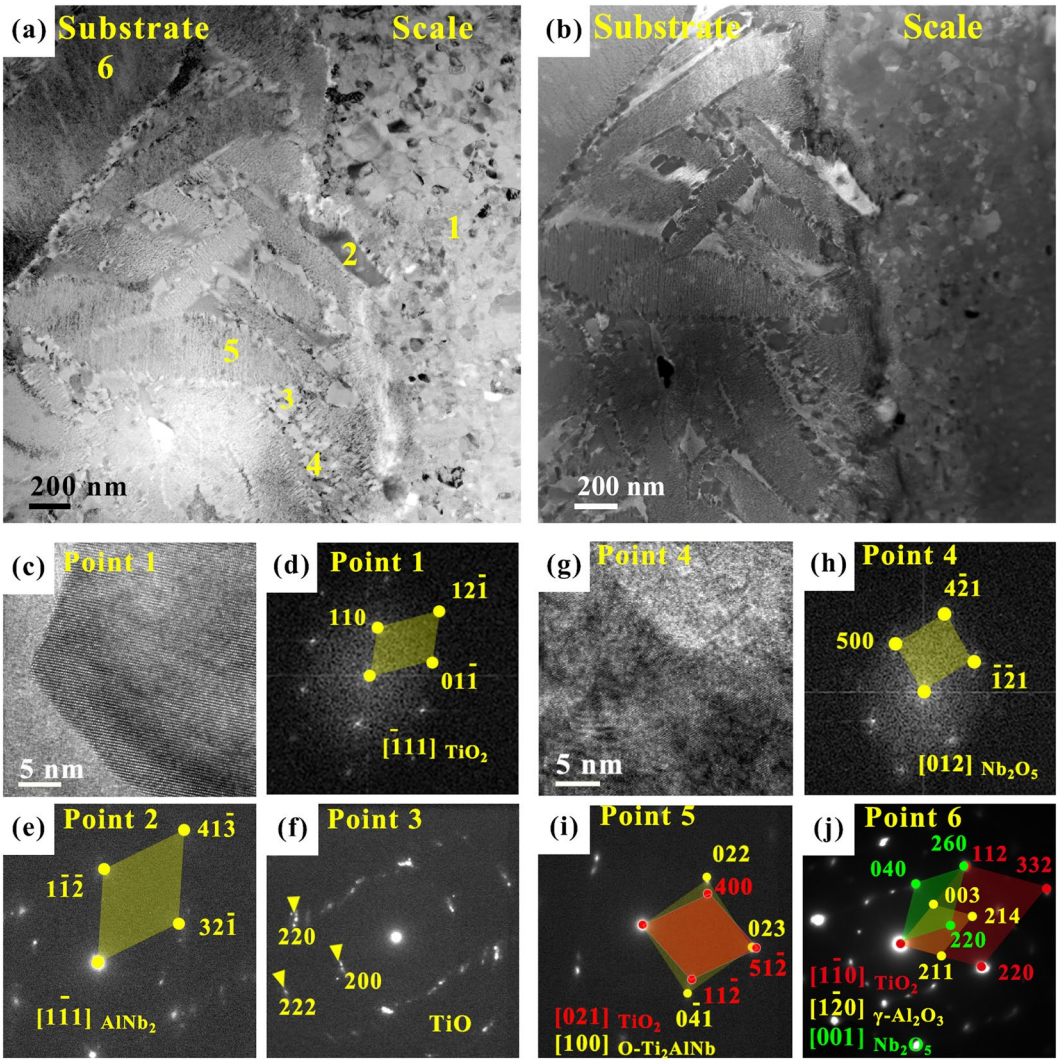

Figure 4. Microstructures of interface between as-cast Ti_2AlNb-based alloy substrate and oxide scale. (**a**) TEM bright field image of interface, where white regions reflect pores, (**b**) high angle annular dark field (HAADF) image of (**a**); (**c**) HRTEM of point 1, and (**d**) FFT image of (**c**); (**g**) HRTEM of point 4, and (**h**) FFT image of (**g**); (**e**), (**f**), (**i**) and (**j**) the corresponding SAED patterns of points 2, 3, 5, 6, where point 1 represents rutile-TiO_2, point 2 represents $AlNb_2$, point 3 represents TiO, point 4 represents Nb_2O_5, point 5 represents brookite TiO_2 and O-Ti_2AlNb phase, point 6 represents rutile TiO_2, Nb_2O_5 and γ-Al_2O_3.

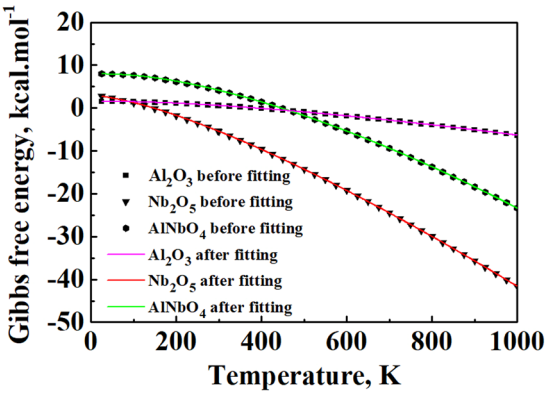

Figure 5. Gibbs free energy curves of Al_2O_3, Nb_2O_5 and $AlNbO_4$ before and after fitting.

Phase	H_0	a	b	c	I	Adj. R-Square
Al_2O_3	1.18577	−0.00368	−1.4271E-6	3.88868	0.01932	1
Nb_2O_5	2.0799	−0.01388	−2.54067E-6	10.8132	0.05475	1
$AlNbO_4$	6.74954	−0.01287	−8.12388E-6	16.08122	0.06692	0.99999

Table 2. Fitting results of free energy curve of Al_2O_3, Nb_2O_5 and $AlNbO_4$ in Fig. 5.

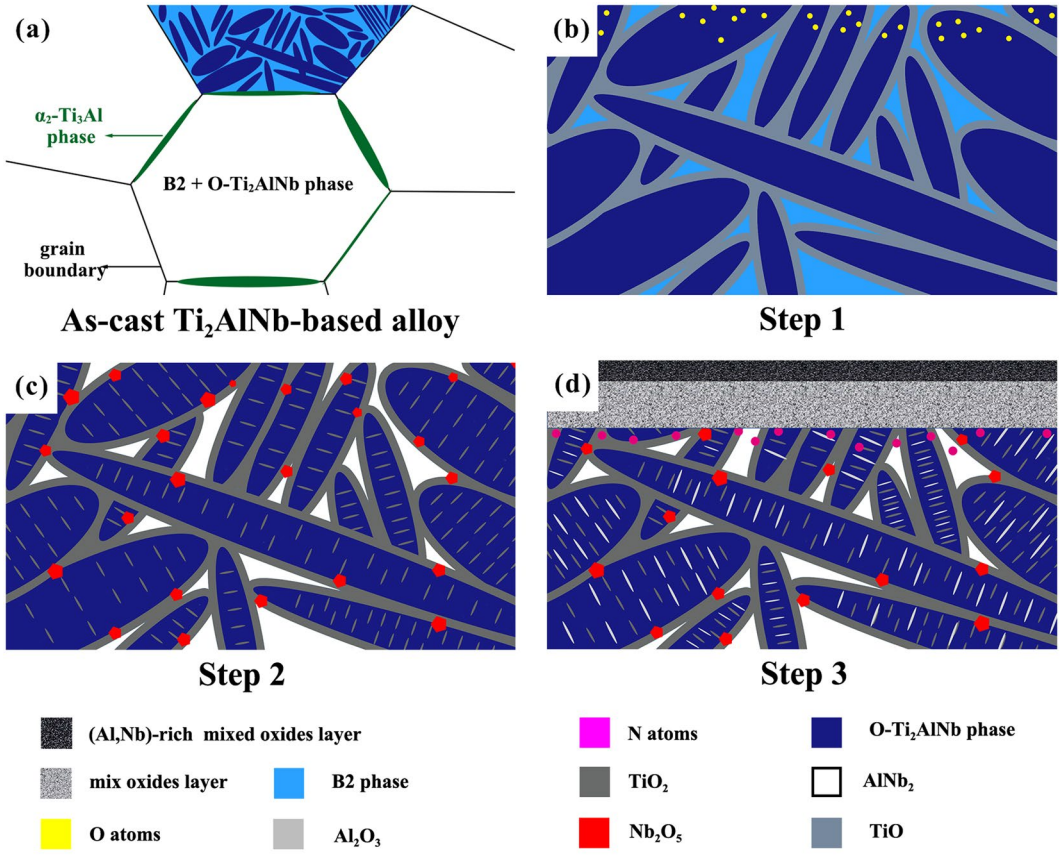

Figure 6. Schematic diagram showing a summary of high-temperature oxidation process of Ti_2AlNb-based alloy. Stage 1, by inward diffusion of oxygen B2 phase is transformed into TiO, and O-Ti_2AlNb is abound with oxygen. Stage 2, TiO is transformed into rutile-TiO_2 and $AlNb_2$ is formed in the areas of B2 phase. Oxidation occurs in O-Ti_2AlNb phase. Stage 3, O-Ti_2AlNb phase breaks down into Al_2O_3, Nb_2O_5 and TiO_2. Al_2O_3 reacts with Nb_2O_5 to form ($AlNbO_4 + TiO_2$) mixed oxide layer. At last, nitrogen dissolves in the alloy.

$$G = H_0 + aT\ln T + bT^2 + \frac{c}{T} + IT, \tag{2}$$

where H_0, a, b, c, and I are fitting parameters. The results show an excellent matching close to 100%, as shown in Fig. 5 and Table 2. The relationships between the Gibbs free energy and temperature for Al_2O_3, Nb_2O_5, and $AlNbO_4$ can thus be expressed as follows,

$$G_{Al_2O_3} = 1.18577 - 0.00368T\ln T - 1.4271 \times 10^{-6}T^2 + \frac{3.88868}{T} + 0.01932T, \tag{3}$$

$$G_{Nb_2O_5} = 2.07990 - 0.01388T\ln T - 2.54067 \times 10^{-6}T^2 + \frac{10.8132}{T} + 0.05475T, \tag{4}$$

$$G_{AlNbO_4} = 6.74954 - 0.01287T\ln T - 8.12388 \times 10^{-6}T^2 + \frac{16.08122}{T} + 0.06692T. \tag{5}$$

Phase	PDF number	Space group	Crystal system
$AlNbO_4$	#41-0347	C2/m (12)	Monoclinic
γ-Al_2O_3	#10-0425	Fd-3m (227)	Cubic
δ-Al_2O_3	#11-0517	C2/m (12)	Monoclinic
α-Al_2O_3	#46-1212	R-3c (167)	Hexagonal
Rutile-TiO_2	#21-1276	P42/mnm (136)	Tetragonal
Brookite-TiO_2	#29-1360	Pcab (61)	Orthorhombic
Nb_2O_5	#22-1196	A2/m (12)	Monoclinic
	#19-0864	Primitive	Monoclinic
$AlNb_2$	#15-0598	P42/mnm (136)	Tetragonal

Table 3. Crystallographic structure of the related oxides.

Substituting $T = 1073.15$ K into the above equations yields the Gibbs free energy values for the formation of Al_2O_3, Nb_2O_5, and $AlNbO_4$, respectively, in the present oxidation condition of a higher temperature. As a result, the Gibbs free energy change of the reaction $Nb_2O_5 + Al_2O_3 \rightarrow 2AlNbO_4$ becomes -1.00873 kJ/mol. This means that the reaction is thermodynamically possible. Also, Ai *et al.*[52] reported that Nb_2O_5 reacted completely with Al_2O_3 to form $AlNbO_4$ in Nb_2O_5-Al_2O_3 ceramics. While Nb_2O_5 is consumed as a reactant, the formed $AlNbO_4$ makes the scale unprotective as well[14]. Furthermore, Nb_2O_5 is not observed in the XRD results (Fig. 2(c)), which can be mainly attributed to its reaction with Al_2O_3 as discussed above, in conjunction with the lower diffusion coefficient of Nb, the rapid growth of TiO_2, and the hindering effect of alumina.

Oxidation process at the interface. Based on the above observations and analyses, the high-temperature oxidation process of the Ti_2AlNb-based alloy can be summarized below and schematically shown in Fig. 6. Stage 1: Oxygen absorbs on the surface of the Ti_2AlNb-based alloy, which later penetrates into it. The B2 phase is oxidized to produce TiO, and oxygen dissolves in O-Ti_2AlNb phase. Stage 2: TiO is transformed into rutile-TiO_2 and $AlNb_2$ is formed in the areas of the B2 phase. Oxidation occurs, i.e., brookite-TiO_2 is generated inside the O-Ti_2AlNb phase and Nb_2O_5 outside the O phase. Stage 3: O-Ti_2AlNb phase breaks down to TiO_2, Nb_2O_5, and Al_2O_3. In the scale there is a reaction: $Al_2O_3 + Nb_2O_5 \rightarrow 2AlNbO_4$, and N atoms are dissolved in the alloy because of the consumption of O atoms. The corresponding crystallographic structures of the related oxides of the Ti_2AlNb-based alloy are summarized in Table 3.

Conclusions

1. After being exposed at 800 °C in static air for 100 h, the Ti_2AlNb-based alloy followed an almost liner kinetic law of oxidation and exhibited a multi-layered structure consisting of an (Al,Nb)-rich mixed oxide layer (I), mixed oxide layer (II), and oxygen-rich layer (III) from the outside to inside.
2. In the mixed outer scale, there existed α-Al_2O_3 and δ-Al_2O_3. Al_2O_3 reacted with Nb_2O_5 to form $AlNbO_4$, however, Nb_2O_5 and $AlNbO_4$ were not able to hinder the diffusion of oxygen.
3. The B2 phase was oxidized to form TiO_2, where Nb and Al were transformed into $AlNb_2$ at the interface during oxidation. $AlNb_2$ could hinder the diffusion of oxygen and improve the oxidation resistance of the Ti_2AlNb-based alloy, but its discontinuous nature allowed only a limited effect.
4. After long-term oxidation at 800 °C, O-Ti_2AlNb was oxidized to form TiO_2, Al_2O_3 and Nb_2O_5. Al_2O_3 could hinder the growth of TiO_2 in the O-Ti_2AlNb laths and form a compact scale. Increasing the amount of the O-Ti_2AlNb phase in the alloy contributes to the improvement in its high-temperature oxidation resistance.

Data Availability. The datasets generated and/or analyzed during the current study are available from the corresponding author on reasonable request.

References

1. Banerjee, D., Gogia, A. K., Nandi, T. K. & Joshi, V. A. A new ordered orthorhombic phase in a Ti_3Al-Nb alloy. *Acta Metall* **36**, 871–882 (1988).
2. Muraleedharan, K., Gogia, A. K., Nandy, T. K., Banerjee, D. & Lele, S. Transformations in a Ti-24Al-15Nb alloy: Part 1. Phase equilibria and microstructure. *Metall Trans* **23A**, 401–415 (1992).
3. Bendersky, L. A., Boettinger, W. J. & Roytburd, A. Coherent precipitates in the b.c.c./orthorhombic two-phase field of the Ti-Al-Nb system. *Acta Metall Mater* **39**, 1959–1969 (1991).
4. Muraleedharan, K., Banerjee, D., Banerjee, S. & Lele, S. The a_2-to-O transformation in Ti-Al-Nb alloys. *Philos. Mag. A* **71**, 1011–1036 (1995).
5. Vasudevan, V. K., Yang, J. & Woodfield, A. P. On the β to B2 ordering temperature in a Ti-22Al-26Nb orthorhombic titanium aluminide. *Scripta Mater.* **35**, 1033–1039 (1996).
6. Banerjee, D. The intermetallic Ti_2AlNb. *Prog Mater Sci* **42**, 135–158 (1997).
7. Sarosi, P. M., Hriljac, J. A. & Jones, I. P. Atom location by channelling-enhanced microanalysis and the ordering of Ti_2AlNb. *Philos Mag* **83**, 4031–4044 (2003).
8. Zhang, L. T., Ito, K., Inui, H., Vasudevan, V. K. & Yamaguchi, M. Microstructures with martensitic features induced by absorption of a large amount of hydrogen in a B2 single-phase Ti-22Al-27Nb alloy. *Acta Mater* **51**, 781–788 (2003).

9. Jiao, X., Liu, G., Wang, D. & Wu, Y. Creep behavior and effects of heat treatment on creep resistance of Ti-22Al-24Nb-0.5Mo alloy. *Mater Sci Eng A* **680**, 182–189 (2017).
10. Wu, Y., Liu, G., Jin, S. & Liu, Z. Microstructure and mechanical properties of Ti_2AlNb cup-shaped part prepared by hot gas forming: determining forming temperature, strain rate, and heat treatment. *Int. J. Adv. Manuf. Tech.* **92**, 4583–4594 (2017).
11. Zhao, H., Lu, B., Tong, M. & Yang, R. Tensile behavior of Ti-22Al-24Nb-0.5Mo in the range 25–650°C. *Mater. Sci. Eng., A* **679**, 455–464 (2017).
12. Leyens, C. & Gedanitz, H. Long-term oxidation of orthorhombic alloy Ti-22Al-25Nb in air between 650 and 800 °C. *Scripta Mater.* **41**, 901–906 (1999).
13. Kumpfert, J. Intermetallic alloys based on orthorhombic titanium aluminide. *Adv Eng Mater* **3**, 851–864 (2001).
14. Leyens, C. Oxidation of orthorhombic titanium aluminide Ti-22Al-25Nb in air between 650 and 1000 °C. *JMEPEG, ASM International* 10, (225–230 (2001).
15. Germann, L., Banerjee, D., Guédou, J. Y. & Strudel, J. L. Effect of composition on the mechanical properties of newly developed Ti_2AlNb-based titanium aluminide. *Intermetallics* **13**, 920–924 (2005).
16. Dang, W., Li, J., Zhang, T. & Kou, H. Microstructure and phase transformation in Ti-22Al-(27-x)Nb-xZr alloys during continuous heating. *J. Mater. Eng. Perform.* **24**, 3951–3957 (2015).
17. Gong, X. *et al*. Synergistic effect of B and Y on the isothermal oxidation behavior of TiAl-Nb-Cr-V alloy. *Corros. Sci.* **131**, 376–385 (2018).
18. Taniguchi, S., Shibata, T. & Sakon, S. Oxidation resistance of TiAl significantly improved by combination of preoxidation and Hf addition. *Mater. Sci. Eng., A* **A198**, 85–90 (1995).
19. Braun, R. & Leyens, C. Protective coatings on orthorhombic Ti_2AlNb alloys. *Mater. High Temp.* **22**, 437–447 (2005).
20. Xiong, Y. M., Zhu, S. L. & Wang, F. H. The oxidation behavior of TiAlNb intermetallics with coatings at 800 °C. *Surf. Coat. Technol.* **197**, 322–326 (2005).
21. Wang, Q. M. *et al*. NiCoCrAlY coatings with and without an Al_2O_3/Al interlayer on an orthorhombic Ti_2AlNb-based alloy: Oxidation and interdiffusion behaviors. *Acta Mater* **55**, 1427–1439 (2007).
22. Goral, M., Moskal, G., Swadzba, L. & Tetsui, T. Si-modified aluminide coating deposited on TiAlNb alloy by slurry method. *Journal of Achievements in Materials and Manufacturing Engineering* **21**, 75–78 (2007).
23. Li, H. Q., Wang, Q. M., Jiang, S. M., Gong, J. & Sun, C. Ion-plated Al-Al_2O_3 films as diffusion barriers between NiCrAlY coating and orthorhombic-Ti_2AlNb alloy. *Corros. Sci.* **52**, 1668–1674 (2010).
24. Li, H. Q. *et al*. Oxidation and interfacial fracture behaviour of NiCrAlY/Al_2O_3 coatings on an orthorhombic-Ti_2AlNb alloy. *corros. Sci.* **53**, 1097–1106 (2011).
25. Shi, J., Li, H. Q., Wan, M. Q., Wang, H. L. & Wang, X. High temperature oxidation and inter-diffusion behavior of electroplated Ni-Re diffusion barriers between NiCoCrAlY coating and orthorhombic-Ti_2AlNb alloy. *Corros. Sci.* **102**, 200–208 (2016).
26. Gong, X. *et al*. Effect of Mo on microstructure and oxidation of NiCoCrAlY coatings on high Nb containing TiAl alloys. *Appl. Surf. Sci.* **431**, 81–92 (2018).
27. Wang, Y.-H., Ouyang, J.-H., Liu, Z.-G., Wang, Y.-M. & Wang, Y.-J. Microstructure and high temperature properties of two-step voltage-controlled MAO ceramic coatings formed on Ti_2AlNb alloy. *Appl. Surf. Sci.* **307**, 62–68 (2014).
28. Stoloff, N. S. *Environmental embrittlement, in Physical Metallurgy and Processing of* Intermetallic *Compounds. (ed. Stoloff, N.S., Sikka, V.K.)*. 479–516 (Springer US, 1996).
29. Lu, W., Chen, C. L., Xi, Y. J., Wang, F. H. & He, L. L. The oxidation behavior of Ti-46.5Al-5Nb at 900 °C. *Intermetallics* **15**, 989–998 (2007).
30. Zhu, H. P., Qu, S. J., Qi, G. Y. & Shen, J. High temperature oxidation behavior of as-rolled Ti_2AlNb-based alloy. *China. J. Rare Metals* **40**, 104–109 (2016).
31. Lee, D. B. Effect of Cr, Nb, Mn, V, W and Si on high temperature oxidation of TiAl alloys. *Met. Mater. Int.* **11**, 141–147 (2005).
32. Birks, N., Meier, G. H. & Pettit, F. S. *Introduction to the high temperature oxidation of metals*. 23 (Cambridge University Press, 2006).
33. Yoshihara, M. & Miura, K. Effects of Nb addition on oxidation behavior of TiAl. *Intermetallics* **3**, 357–363 (1995).
34. Jiang, H., Hirohasi, M., Lu, Y. & Imanari, H. Effect of Nb on the high temperature oxidation of Ti-(0-50 at.%)Al. *Scripta Mater.* **46**, 639–643 (2002).
35. Lu, W., Chen, C., He, L., Xi, Y. & Wang, F. Effect of niobium on the oxidation behavior of TiAl. *J. Mater. Res.* **22**, 1486–1490 (2007).
36. Vojtěch, D., Čížkovský, J., Novák, P. & Šerák, J. F. Effect of niobium on the structure and high-temperature oxidation of TiAl-Ti_5Si_3 eutectic alloy. *Intermetallics* **16**, 896–903 (2008).
37. Lin, J. P. *et al*. Effect of Nb on oxidation behavior of high Nb containing TiAl alloys. *Intermetallics* **19**, 131–136 (2011).
38. Ralison, A., Dettenwanger, F. & Schütze, M. Oxidation of orthorhombic Ti_2AlNb alloys at 800°C in air. *Mater. Corros.* **51**, 317–328 (2000).
39. Ralison, A., Dettenwanger, F. & Schütze, M. Oxidation of orthorhombic Ti_2AlNb alloys in the temperature range 550–1000 °C in air. *Mater. High. Temp.* **20**, 607–629 (2003).
40. Zheng, D. Y., Xiong, Y. M., Zhu, S. L., Li, M. S. & Wang, F. H. Oxidation and hot corrosion behavior of T_i2AlNb-based alloy with and without enamel coating at 80 °C. *Trans. Nonferrous Met. Soc. China* **16**, s2050–s2054 (2006).
41. Malecka, J. Investigation of the oxidation behavior of orthorhombic Ti_2AlNb alloy. *J. of Mater. Eng. Perform.* **24**, 1834–1840 (2015).
42. Li, H. Q., Wang, Q. M., Gong, J. & Sun, C. Interfacial reactions and oxidation behavior of Al_2O_3 and Al_2O_3/Al coatings on an orthorhombic Ti_2AlNb alloy. *Appl. Surf. Sci.* **257**, 4105–4112 (2011).
43. Leyens, C. & Peters, M. *Titanium and titanium alloys. Fundamentals and applications*., 1–513 (Wiley-VCH GmbH & Co. KGaA, Weinheim., 2003).
44. Becker, S., Rahmel, A., Schorr, M. & Schütze, M. Mechanism of isothermal oxidation of the intermetallic TiAl and of TiAl alloys. *Oxid. Met.* **38**, 425–464 (1992).
45. Qu, S. J. *et al*. Microstructural evolution and high-temperature oxidation mechanisms of a titanium aluminide based alloy. *Acta Mater* **148**, 300–310 (2018).
46. Dettenwanger, F., Schumann, E., Ruhle, M., Rakowski, J. & Meier, G. H. Microstructural study of oxidized gamma-TiAl. *Oxid. Met.* **50**, 269–307 (1998).
47. Lu, W. *et al*. (S)TEM study of different stages of Ti-45Al-8Nb-0.2W-0.2B-0.02Y alloy oxidation at 900 degrees C. *Corros. Sci.* **50**, 978–988 (2008).
48. Yang, J. C., Schumann, E., Levin, I. & Ruhle, M. Transient oxidation of NiAl. *Acta Mater* **46**, 2195–2201 (1998).
49. Cowley, J. M. Stacking faults in gamma-alumina. *Acta Cryst.* **6**, 53–54 (1953).
50. Engelhart, W., Dreher, W., Eibl, O. & Schier, V. Deposition of alumina thin film by dual magnetron sputtering: Is it g-Al_2O_3? *Acta Mater* **59**, 7757–7767 (2011).
51. Levin, I. & Brandon, D. Metastable alumina polymorphs: Crystal structures and transition sequences. *J. Am. Ceram. Soc.* **81**, 1995–2012 (1998).
52. Ai, Y. L., He, F., Liang, B. L., He, W. & Liu, L. Hydrochloric acid corrosioin behavior of Nb_2O_5-Al_2O_3 ceramics prepared by microwave sintering. *Adv. Mater. Res.* **418-420**, 55–58 (2012).

Acknowledgements

The authors are grateful for the financial support provided by the National Natural Science Foundation of China (NSFC) (Grant Nos U1302275, 51471155 and 51305304) and the Natural Sciences and Engineering Research Council of Canada (NSERC) in the form of international research collaboration, Fundamental Research Funds for the Central Universities, and Major Science and Technology Project "High-end CNC Machine Tools and Basic Manufacturing Equipment" (2013ZX04011061). One of the authors (D.L. Chen) is also grateful for the financial support by the Premier's Research Excellence Award (PREA), NSERC-Discovery Accelerator Supplement (DAS) Award, Canada Foundation for Innovation (CFI), and Ryerson Research Chair (RRC) program. The authors also thank Prof. G.J. Cao of Harbin University of Science and Technology, for his assistance in the TEM/HRTEM observations.

Author Contributions

J.M. Xiang conducted the oxidation experiments. S.J. Qu and J. Shen designed and supervised the project, and produced the samples. J.M. Xiang, S.J. Qu, G.B. Mi, A.H. Feng, X. Huang, Z. Chen, J. Shen, and D.L. Chen analyzed the data. J. Shen and D.L. Chen assessed the outcome. J.M. Xiang, S.J. Qu, G.B. Mi, A.H. Feng and D.L. Chen wrote the paper. All the authors discussed the results and commented on the manuscript.

Additional Information

Competing Interests: The authors declare no competing interests.

Publisher's note: Springer Nature remains neutral with regard to jurisdictional claims in published maps and institutional affiliations.